Nonlinear Dyn
https://doi.org/10.1007/s11071-024-09864-6

RESEARCH

Leveraging systems' non-linearity to tackle the scarcity of data in the design of intelligent fault diagnosis systems

Giancarlo Santamato · Andrea Mattia Garavagno · Massimiliano Solazzi · Antonio Frisoli

Received: 5 February 2024 / Accepted: 8 June 2024

Abstract Deep transfer learning (DTL) allows for the efficient building of intelligent fault diagnosis systems (IFDS). On the other hand, DTL methods still heavily rely on large amounts of labelled data. Obtaining such an amount of data can be challenging when dealing with machines or structures faults. This document proposes a novel approach to the design of vibration-based IFDS using DTL in condition of strong data scarcity. A periodic multi-excitation level procedure leveraging intrinsic non-linearities of real-world systems is used to produce images that can be conveniently analysed by pre-trained Convolutional Neural Networks to diagnose faults. A new data visualization method and its augmentation technique are proposed in this paper to tackle the typical lack of data encountered during the design of IFDS. Experimental validation on a railway pantograph structure provides effective support for the proposed method.

Keywords Structural health monitoring · Intelligent fault diagnosis systems · Deep transfer learning · Data augmentation

1 Introduction

Deep transfer learning (DTL) is enabling the rise of the next-generation machine and structural health monitoring systems [3]. The advantage of Deep Learning (DL) in feature representation combined with the ability to reuse the knowledge extracted from large datasets, typical of Transfer Learning, allows for the efficient building of intelligent fault diagnosis systems (IFDS). On the other hand, DTL methods heavily rely on large amounts of labeled data. Nevertheless, few works propose techniques to tackle the typical data scarcity encountered when designing IFDS in real-world scenarios. Hence, addressing the data lack is still an open issue [21].

The present document proposes a novel data augmentation and visualization technique leveraging structures' nonlinearity to tackle strong data scarcity.

The proposed approach belongs to the so-called non-parametric techniques, meaning that it only relies on features that are extracted directly from raw data with no need for physical models. In particular, this technique is suitable for structural dynamic tests where the excitation level can be controlled externally.

Giancarlo Santamato and Andrea Mattia Garavagno contributed equally to this work.

G. Santamato (✉) · A. M. Garavagno · M. Solazzi · A. Frisoli
Institute of Mechanical Intelligence, Scuola Superiore Sant'Anna, via Alamanni 13b, Ghezzano, 56010 Pisa, Italy
e-mail: giancarlo.santamato@santannapisa.it

A. M. Garavagno
e-mail: andreamattia.garavagno@santannapisa.it

G. Santamato · A. M. Garavagno · M. Solazzi · A. Frisoli
Department of Excellence in Robotics & AI, Scuola Superiore Sant'Anna, Pisa, Italy
e-mail: massimiliano.solazzi@santannapisa.it

A. Frisoli
e-mail: antonio.frisoli@santannapisa.it

Published online: 04 July 2024

In particular, the input–output response of the structure is conveyed through the Frequency Response Function (FRF) acquired at different excitation levels and collected in a single color map, thus producing a spectrogram-like image where the axis of time is substituted by the axis of the excitation level. Such a representation enables a novel custom procedure of data augmentation, where different acquisitions of the same fault are mixed to create a multitude of new realistic color maps, thus leveraging the excitation level multiplicity.

The performance of the proposed technique is investigated experimentally through dedicated structural dynamics tests performed on a railway pantograph mechanism, as an example of an inherently nonlinear system owing to dry-frictional nonlinearity [34]. Two damage scenarios, namely the loss of member connectivity at a bolted connection and tampering of the artificial damping, have been tested while the excitation varied on seven levels, ranging over one order of magnitude and stimulating stuck and stick–slip regimes. The collected data is visualized and augmented using the proposed technique and then used to train a bi-dimensional Convolutional Neural Network (CNN) for performing intelligent fault diagnosis. Therefore we show how the resulting IFDS can correctly classify the undamaged condition and the fault scenarios with a relatively low-size data set. Ablation studies are conducted to demonstrate the importance of the proposed data augmentation technique while designing the proposed IFDS.

The paper is structured as follows: a survey of the literature delving with non-parametric fault diagnosis is reviewed from classical approaches to AI methods in Sect. 2. The context of the research, arising from an industrial project is introduced in Sect. 3. The proposed approach is presented in Sect. 4 as long as the assumed hypotheses and assumptions. Section 5 is devoted to describing the experimental tests performed on a railway pantograph and discussing the fault diagnosis performance achieved through our IFDS. Three ablation studies are presented in Sect 6. Section 7 synthesizes the work and highlights future developments.

2 Related work

Vibration-based IFDSs are often found in the scientific literature [3]. Classical approaches often utilized the experimental estimate of the Frequency Response Function (FRF) as a numerical series [18]. In the Waveform Chain Code (WCC) approaches, the damage index is obtained by summing up the contributions of the absolute difference between the first and/or second derivatives of the FRFs series in the damaged and undamaged conditions [4]. The FRF-based curvature method was proved to successfully identify and locate multiple damage sites in a steel beam [30]. The WCC can also be performed on Principal Component Analysis (PCA)-reduced FRFs. In [7,8] k-means unsupervised clustering with unlabeled data allowed to separate with high-accuracy damage conditions such as screws removed or loosened. The Interpolation Damage Detection Method (IDDM) was utilized on bridges and frame structures to detect early damages and location, in the presence of noise and environmental changes [26,27]. The FRF Similarity Metric (FRFSM) was proposed in [20] as a statistical method to compare the dB-scale magnitude of two FRFs, based on the probability density function of normal distribution in the frequency domain.

Nevertheless, many engineering structures are inherently nonlinear due to complex joints and interfaces, such as the presence of dry-friction at the connections. Consequently, the characteristics of the structure not only in the undamaged but also in the damaged condition can be found dependent on the excitation amplitude, based on whether the external excitation breaks the joints friction. However, few existing algorithms consider nonlinear structural behavior in the reference and damaged states [15]. In this regard, [37] demonstrated numerically and experimentally that the damage signature is dependent on the friction-over-excitation ratio also in a statistical sense. The relevance of the input excitation level was supported by numerous experimental tests, performed on a railway pantograph structure, and discussed for several kinds of defects [34] through the analysis of the FRF through classical statistical analysis based on a p-value formulation.

Big data techniques like Support Vector Machines [1,56], decision trees [25], Random Forests (RF) [45], k-nearest neighbors (KNN) [42] and dictionary-based learning [44,55], as well as deep learning ones like Auto Encoders (AEs) [39], Deep Belief Networks (DBN) [40], Recurrent Neural Networks (RNNs) [11, 54], Spiking Neural Networks (SNNs) [58], General Adversial Networks (GANs) [57] [23], Swin Transformers [53], one-dimensional CNNs [24] and bi-

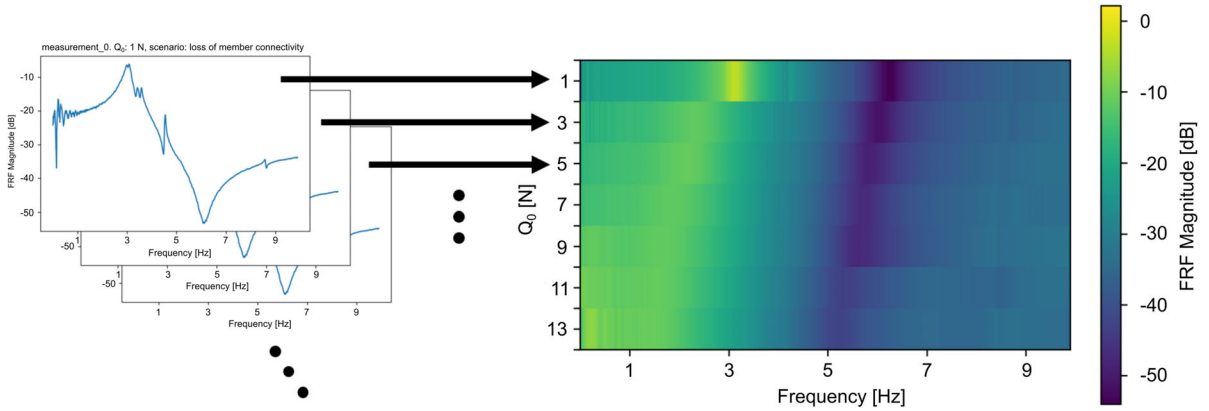

Fig. 1 A figure of the proposed visualization method. The Frequency Response Functions (FRF) acquired at each excitation level are on the rows of the color map. The excitation levels are reported on the y-axis, while the frequencies on the x-axis. The corresponding magnitude is reported in the color map legend. Yellowish colors indicate peaks of the FRF, while blueish colors indicate minima

dimensional CNNs [2] are also used to diagnose faults, often in combination with classical techniques.

In the case of IFDS based on bi-dimensional CNNs, like the proposed method, acquired time series are transformed into images. Techniques like short-time Fourier transform (STFT) [29,43,47,52] and Wavelet Transform (WT) [12–14,16] are widely applied to produce spectrogram images. Time series are also visualized as images in polar coordinates applying the principle of symmetrized dot pattern [41], or as bi-dimensional Kurtograms [31]. Sometimes the samples directly become the pixel of a grayscale image [51], or time series coming from different sensors compose a bi-dimensional matrix [49]. Moreover, a visualization technique based on the PE has been proposed [19]. It uses non-uniform embedding of the vibration signal into a delay coordinate space with variable time lags to produce images. Another approach that does not require visualization techniques consists of capturing vibration images using event-based cameras, as proposed in [9,22].

The visualization method on which the proposed augmentation technique is based does not use any of the previously cited visualization techniques. It visualizes the FRFs obtained at different excitation levels in the same 2D image as a color map. The resulting images, as shown in Fig. 1, resemble a spectrogram with the main difference of representing the variations of the frequency response function with respect to different excitation levels, instead of the time.

3 Background: case study

The present research arises from the *Trenitalia project*, during which we developed portable testing equipment and advanced methodologies for railway pantograph inspection and maintenance.

A railway pantograph, shown in Fig. 3, is a deployable linkage mechanism installed on electric trains to collect power from the high-voltage line. Consequently, in-depth inspection is essential to enhance the service continuity and safety of railway traffic.

In this regard, the standard approach to damage detection is using a vibration-based technique [5,6], in which external devices are used to induce a controlled vibration pattern on the structure to collect and process the output response. Conventional routines at the State-of-the-Art [50] reconstruct the FRF which is then processed and compared with the corresponding labeled FRF of the undamaged pantograph structure.

Nevertheless, recent research [34] proved that railway pantographs, as the majority of linkage structures are *inherently nonlinear*, i.e. exhibit nonlinear behavior also in the undamaged state. Consequently, classical FRF-based approaches are inadequate.

What is more, the presence of dry-friction at joints implies a dependence of the response also on the experimental test boundary conditions, such as the starting reference position of the structure, the exact value of the pre-stress in the suspension, and even slight variation in the linkage positions induced by play.

In view of this, traditional statistical approaches do not guarantee high levels of confidence in the detection and identification exercises while DTL techniques may represent an interesting alternative approach. On the other side, the development of detection algorithms requires the availability of substantial labeled data, associated with the undamaged and the possible damaged conditions. Nevertheless, adequate dataset collection is challenging due

- To the scarcity of pantograph samples that could be available for deep experimental tests;
- The long time needed to set up the characterization campaign which also needs adequate facilities and personnel;
- The large number of fault cases that should be simulated for testing.

Consequently, solutions to tackle the scarcity of data are crucial to exploit the potential of Deep Learning in the damage detection process. The development of a data augmentation technique, exploiting the inherent nonlinearity of linkage structures is the main concern of the present research paper.

4 The proposed approach to Intelligent Fault Diagnosis

The proposed approach uses a vibration-based multilevel excitation procedure to produce images representing the FRF of the structure under test, which is stimulated with an external excitation $q(t)$, artificially generated by dedicated equipment, and which can be eventually combined with environmental sources.

4.1 Hypotheses and assumptions

The application of our methodology relies on a fundamental assumption, that is inherent nonlinearity, which implies that the structural response is dependent on the vibration amplitude both in the undamaged and damaged condition. Despite the assumption of nonlinear behavior, the eligibility of the FRF still holds for the purpose of intelligent fault diagnosis.

When nonlinearity is present, the spectral content of the response $x(t)$ under a harmonic excitation at a frequency ρ_d is in general spread over a multitude of frequency bins other than the excitation frequency ρ_d. Nonetheless, in many cases, like Coulomb friction nonlinearity, the magnitude of these spurious harmonics is found negligible compared to the excitation frequency. Consequently, the response can be expressed in the frequency domain as follows:

$$X(\rho_d) = \mathcal{F}[x(t)]_{\rho=\rho_d} \tag{1}$$

where $\mathcal{F}$ stands for the Fourier transform. In other words, only the principal harmonic ρ_d can be retained from the entire transform signal.

Such a linearization procedure still holds when the input takes the form of a white-noise signal, i.e. random sequence or chirp waveform, which represent the most common types of excitation in the experimental routines. Hence, a frequency response function can be estimated in the classical non-parametric form, as the ratio of the Fourier transform of the input and output data record [38]:

$$FRF = \frac{\mathcal{F}[x(t)]}{\mathcal{F}[q(t)]} \tag{2}$$

Yet, information about nonlinearity can be retained by carrying out several tests at different levels of the input excitation Q_0 (root-mean-squares, instantaneous amplitude, etc.) [10,28,48]. A further assumption is that the input excitation Q_0 can be tuned at least on two levels.

4.2 The methodology

Let us consider the structure under test to be excited at a given level Q_{01}. In experimental dynamics routines, structural excitation is repeated K times for the sake of statistics, due to the presence of uncertainties.

Consequently, for the given level Q_{01}, we have K estimates of the frequency response function FRF_1^j with $j = 1, ..., K$, that can be stored in the first row of the matrix shown in Fig. 2. Traditional noise mitigation techniques, like the p-Welch algorithm [46], exploit these repetitions to derive an averaged FRF, meaning that K subsequent repetitions contribute to obtain one estimate of the frequency response.

The same procedure is repeated with several excitation levels $Q_{01}, ...Q_{0N}$, where N is the number of chosen excitation levels, with $N \geq 2$. In the end, we

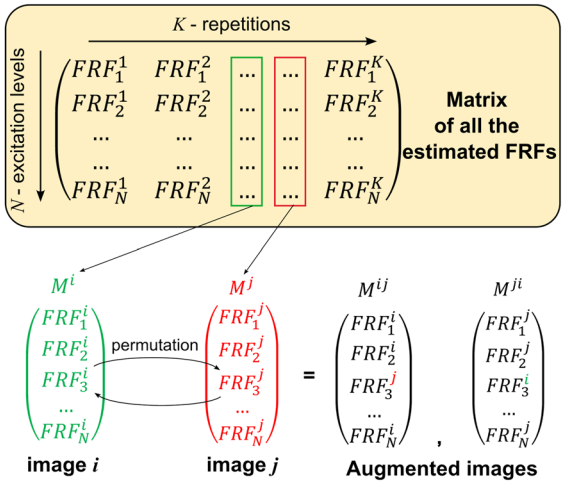

Fig. 2 A graphical representation of the concept behind the proposed data augmentation technique. Two matrices, M^i and M^j are extracted from the whole matrix of FRFs estimated in a given health condition. The permutation of two frequency response FRF_3^i and FRF_3^i, at the same excitation level Q_{03}, creates two additional matrices M^{ij} and M^{ji} that will be plotted as a color map

will have a whole matrix M collecting all the FRF-estimates, with K-columns (number of repetitions), and N-rows (number of excitation levels).

Each column of the matrix M contains the samples of the FRF and it can be plotted in the form of a color map, as shown in Fig. 1, where the excitation levels are on the y-axis, while the frequencies on the x-axis. Lastly, the dB-magnitude of the frequency responses is shown in the color map legend.

At this point, let us consider extracting two generic columns, M^i and M^j from the whole matrix M, and to permute one row, as shown in Fig. 2. Such a swapping operation generates two additional columns M^{ij}, and M^{ji} that can be converted into new images, and hence augmenting the available data. Doing all the swaps allowed with N excitation levels and K repetitions we obtain K^N images, thus augmenting the dataset of a factor K^N/K.

The proposed method has been tested and performed on each condition of the structure under test, including undamaged condition and each damage scenario, as it will be discussed in Sect. 5. Besides, the introduction of the excitation level axis exploits the intrinsic non-linearities of real-world systems. Moreover, the power of pre-trained CNNs on Imagenet [32] is used to analyze such non-linearities in order to diagnose faults, enabling the usage of DTL in the design of IFDS, even in strong data scarcity conditions.

5 Experimental investigation

With the purpose of validating the proposed methodology, we arranged an experimental setup devoted to fault diagnosis tests on a real structure.

5.1 Experimental setup and damage scenarios

The experimental setup, shown in Fig. 3a, consists of:

- A real-scale railway pantograph, as an example of a structure with several dry-friction joints (base encumbrance: 1800 x 1350 mm^2; height of the pan head: 1500 mm, driven point mass: 35 kg);
- A custom exciter, endowed with a stinger actuator, able to set the level of the input excitation at a desired value within the range 1–13 N [36];
- An analog force sensor at the driven-point, embedded with a bending parallelogram amplifier, providing a resolution of $5 \cdot 10^{-3}$ N;
- A digital encoder with a resolution of $5 \cdot 10^{-2}$ mm;
- A 16-bit DAC board and a communication module based on the EtherCAT protocol.

As shown in Fig. 3a, the exciter applies a dynamic force $q(t)$ along the vertical direction, measured by the force sensor, while the measured displacement x of the actuation is admitted as the structural response.

The desired excitation signal is generated by the controller commanding the actuation to generate a linear chirp waveform $q_d(t)$ whose instantaneous amplitude Q_0 is controlled by a closed-feedback loop. The objective of the control is to keep the instantaneous amplitude of the applied force close to Q_0 and constant at each frequency bin even in the presence of disturbances (actuator friction and inertia).

For this work, seven distinct values of the excitation amplitude Q_0 have been considered, ranging from 1 N to 13 N, i.e. $N = 7$. The lowest level was chosen based on the force resolution of the actuation. Indeed, below 1 N, some excitation is still possible but the measurements are affected by a high signal-to-noise ratio. Besides, also the input–output coherence at the resonances drops at about 0.5, meaning poor correlation. On the other side, the highest excitation level is set at the power limit of the actuation.

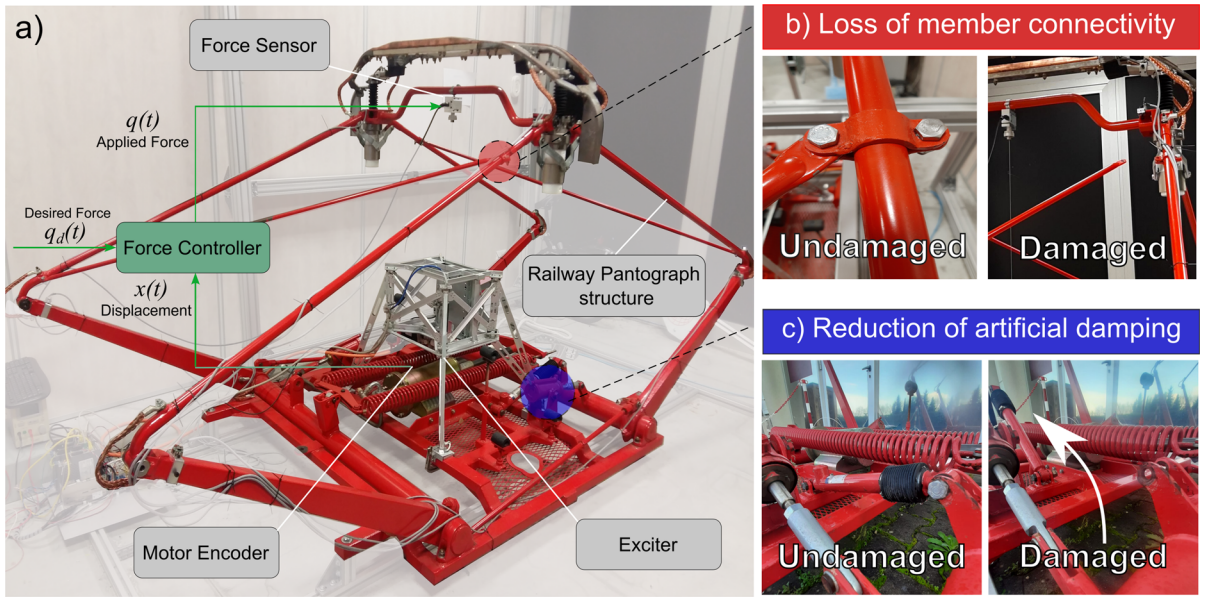

Fig. 3 Experimental setup. (**a**) The structure under test - a railway pantograph - in the test configuration. (**b**) Detail of the bolted connection that has been removed to simulate the loss of member connectivity. (**c**) Detail of the hydraulic dashpot that has been removed to simulate the reduction of artificial damping

All signals are measured with 1000 Hz as the sampling rate. Six repetitions of the dynamic tests have been performed in each scenario ($K = 6$).

European standard [5] and [6] prescribe that validation of pantographs before operational installation, i.e. after overhaul, is executed in the frequency interval 0–20 Hz. In this regard, hydraulic test benches are used during the overhaul to excite the pantograph structure. Nevertheless, we conceived the portable exciter equipment shown in Fig. 3 to perform intermittent inspection of the pantographs outside the overhaul. The bandwidth of such a portable device is considerably lower than rigid test benches, implying that the excitation frequency needs to be restricted to 0–10 Hz to obtain adequate input–output coherence. In this regard, it should be remarked that the substantial signatures of the simulated damages occur below 10 Hz, as demonstrated by the modal analysis in Sect. 5.2 and also by the experimental results shown in Fig. 5.

The pantograph structure endorses several pinned joints with no-lubrication. Consequently, under external excitation, each joints can experience a stuck or a stick–slip regime, based on the local equilibrium forces. Previous studies already demonstrated the nonlinear behavior of the pantograph [34], through the analysis of the FRF estimated for different values of the input excitation. In particular, the overall dry-friction level has been estimated at the driven-point through hysteresis tests, showing a value of hysteretic force equal to 15 N in the absence of other dissipation contributions. It comes that the friction-over-excitation ratio investigated in this study ranges from 1.15 to 15.

In the first explored scenario, we assume the pantograph to be undamaged, and stimulated with the routine described in Sect. 4. Afterward, tests were repeated with the same routine for two simulated damaged scenarios. In particular, we removed the bolted connection of Fig. 3b with the aim of reproducing the loss of member connectivity. It should be considered that bolt removal at this location has no crucial impact on the global integrity due to structural redundancy. Indeed, a twin connection is present on the opposite side of the pantograph. Hence the main effect of this fault is introducing in the explored spectrum the degrees-of-freedom of the diagonal, which can be considered as a local and subtle alteration to structural integrity. In the second damage scenario, we removed the artificial damper, shown in Fig. 3c, by unscrewing one of its pinned connections. In this faulty condition, the overall damping capability of the structure is reduced by 50%

([34],[35]) and the only damping source is due to joints friction.

5.2 Preliminary modal analysis

Before experiments, the effects of the aforementioned damages were theoretically investigated through numerical simulations supported by a finite element model of the pantograph structure, including the suspension organs and the artificial damper. According to the linearity assumption of modal analysis, a frictionless contact condition was assumed for all pinned joints. The loss of member connectivity was simulated by suppressing all the mutual constraints between the diagonal bar and the pantograph frame. For the second damage type, the analysis was repeated setting the damping coefficient equal to zero.

The modal properties within the frequency interval 0–10 Hz are reported in Table 1 in the form of natural frequency Ω in Hz, and percentage modal damping factor ξ. These modes correspond to 99% of the total effective mass and hence provide a complete description of the global mode dynamics of the structure.

Based on the modal results, transient analysis was also performed to estimate numerically the FRF of the pantograph in the three scenarios, as shown in Fig. 4a–c. Therefore, a force load was applied at the driven-point location to simulate the excitation during the test and the response time histories were used to derive the FRF using the same procedure as in the experimental case. To enhance convergence, a numerical damping factor of 0.01% was introduced at all frequencies. This was particularly crucial for the fault-damper scenario for the tampering of the damper implies that in the model no physical damping exists.

The first three modes of the undamaged structure fall within the frequency interval of interest 0–10 Hz, and they involve rigid body motions of the pantograph in the vertical directions while a global bending mode appears in the fourth mode.

The loss of member connectivity introduces two additional resonance peaks at around 4 Hz, while slight frequency shifts are produced on other modes. Such additional modes are reflected in Fig. 4a by the occurrence of two resonance peaks at 3.8 Hz and 4.3 Hz, respectively, while the FRF almost collides with the undamaged case in the other spectrum regions. As shown by the modal shape (normalized to 1) in Fig. 4b,

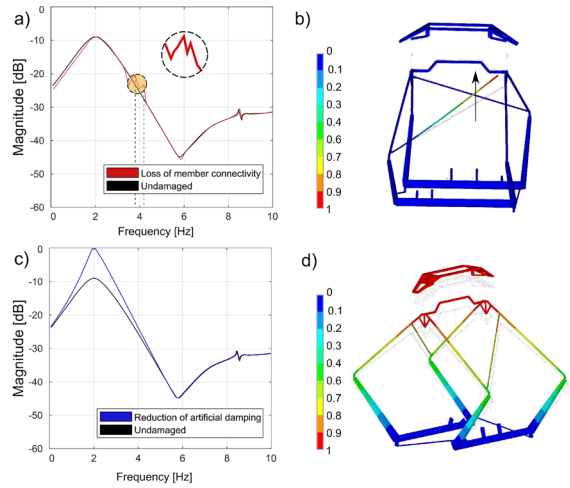

Fig. 4 FEM model of the linkage mechanism (railway pantograph) under test and effects of the simulated damages on the numerical estimate of the FRF. (**a**) Damage in a bolted connection introduces new resonances whose modal shapes have the bending contour shown in (**b**). (**c**) The main effect of the reduction of the artificial damping is a substantial increase of the first resonance peak associated with the vertical oscillation mode shown in (**d**)

when the bolted connection is damaged, the diagonal bar behaves like a cantilever. A first bending oscillation happens with a substantially vertical component of the diagonal tip, at 3.8 Hz, while a mainly lateral oscillation is shown in the second mode.

Instead, the reduction of the artificial damping nullifies the damping factor of the first modes but has no effect on the frequencies. What is more, the damping factor of local modes located at higher frequencies is also unchanged, since the corresponding mode shapes are not related to the artificial damper. As a consequence, the effect of damage in Fig. 4c is concentrated around the first resonance peak of the FRF, corresponding to a large displacement oscillation of the pantograph, as shown in Fig. 4d.

It should be observed that the proposed modal analysis provides useful but indicative information about the dynamic behavior of the structure in undamaged and damaged conditions. The main limitation is indeed related to the assumption of linearity, which neglects the dissipative nonlinear contribution of dry-friction. Besides, such a modal model cannot include the effects of the input excitation on the FRF, such as the variation in the position and magnitude of the resonance peaks as the load-over-friction amplitude increases.

Table 1 Numerical estimate of the modal properties of the railway pantograph under test in the frequency interval of interest (0–10 Hz) in the undamaged, and simulated damaged scenarios

	Mode 1		Mode 2		Mode 3		Mode 4	
Scenario	Ω [Hz]	ξ [%]	Ω [Hz]	ξ [%]	Ω [Hz]	ξ [%]	Ω [Hz]	ξ [%]
Undamaged	2.30	0.31	3.81	0.08	5.02	0.08	8.72	0.02
Loss of member connectivity	2.30	0.31	3.60	0.01	3.79	0.07	4.28	0.02
Reduction of artificial damping	2.30	0.00	3.81	0.00	5.02	0.00	8.72	0.02

5.3 Analysis of the FRFs for multiple levels of the input excitation

For the present study, the experimental FRF was estimated for seven distinct levels of the input excitation: [1, 3, 5, 7, 9, 11, 13] N. The classical periodogram method [46] was applied for the estimate in Eq. 2.

In the undamaged condition, Fig. 5a, the FRF is characterized by a dominant resonance peak and one zero, as confirmed by the theoretical analysis. At the frequency of the dominant peak, the response is magnified, as shown by the yellowish values of the contour map scale. On the contrary, at the frequency of the zero, the structure exhibits no displacement under the effect of the external excitation and the response on the spectrogram is blueish. By increasing the excitation level, both peaks are progressively shifted towards lower frequencies while their amplitude gets more damped. This typical response function is better emphasized in Fig. 5d showing the FRF for an excitation level of 7 N which is collocated at the mean of the explored interval. From such a detail, it also emerges the presence of a further residual peak, at around 4 Hz, very close to the third theoretical mode in Table 1.

As in the theoretical model, the loss of member connectivity, Fig. 5b, introduces two additional resonance peaks which are reflected in the spectrogram by two vertical lines at 3.6 Hz, and 4.6 Hz, respectively. These damage-induce peaks are clearly visible in the detail of Fig. 5e. The interesting point - that cannot be captured by linear modal analysis - is that by increasing the excitation level, the sharpness of the damage-induced resonances is sensibly reduced. As a consequence, the difference between the damaged and the undamaged FRF decreases with the excitation level by a factor of 10.

The reduction of artificial damping, Fig. 5c, implies a shift of the dominant peak with the frequency and an increase of the amplitude. Besides, increasing the excitation level, the FRF exhibits a shifting peak (from 2.6 to 0.5 Hz) and an increase of the amplitude of about 16 dB. Consequently, the difference between the damaged and the undamaged FRF is enhanced by a factor of 10, increasing the excitation level ratio. The different profile of the FRF in this damage scenario is clearly visible in the detail of Fig. 5f, where the dominant peak achieves a value near 0 dB, at a frequency of 1 Hz.

5.4 Design and test of the intelligent fault diagnosis system

5.4.1 Design of the IFDS

To gather the data needed to design the IFDS, an acquisition campaign consisting of three acquisitions for each damage scenario at the seven excitation levels has been performed. The resulting FRFs have been plotted as in Fig. 1, obtaining three images per scenario. The resulting images have been augmented according to the technique proposed in Sect. 4. In this way, $3^7 = 2187$ images were obtained per each scenario, for a total of 6561 images available for the training of the IFDS, of which 20% has been reserved for validation purposes.

Having in mind the long-term objective of deploying the IFDS inside an embedded system to be integrated into the portable testing equipment, we decided to use a pre-trained MobileNetV2 [33] on ImageNet [32] as a feature extractor. The extracted features are reduced by a Global Average Pooling layer which feeds the classifier composed of one dense layer with one neuron per scenario having softmax activation. The classifier is trained for 20 epochs using Adam [17] as optimizer with a learning rate of 10^{-2}. Finally, the whole network is fine-tuned for 10 epochs with a learning rate of 10^{-5} using validation-based early stopping.

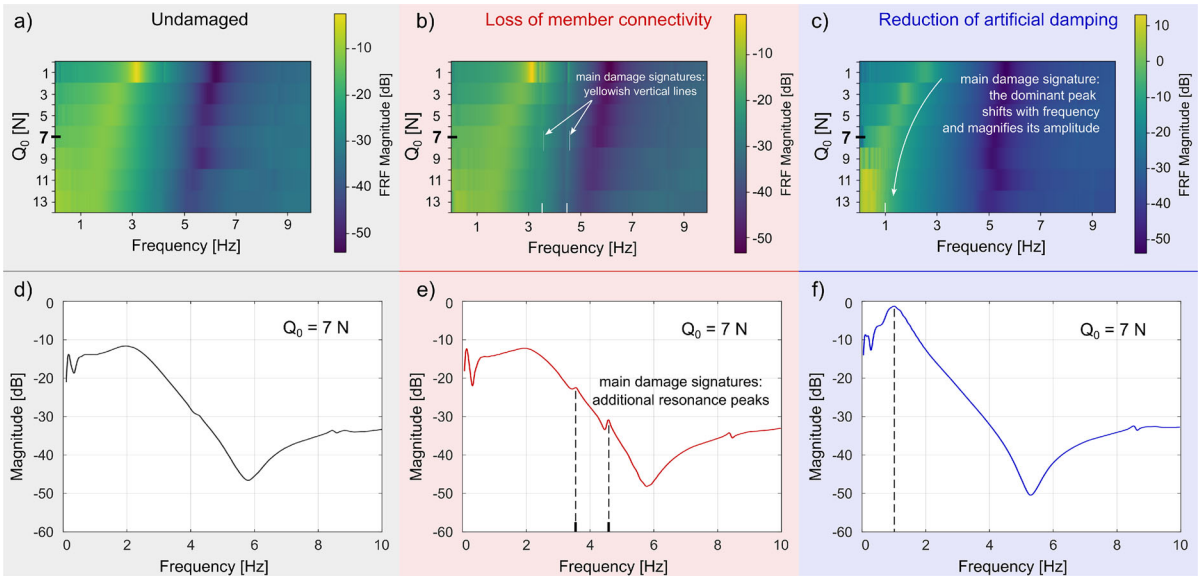

Fig. 5 Color maps of the FRFs in the three explored scenarios: undamaged **a**, loss of bolt connection **b**, and reduction of damper **c**. For each scenario, the FRF are reported below for a value of the external exctiation Q_0 equal to 7 N

5.4.2 Data collection for testing

The same previous modalities were applied to the data collection for testing: a second acquisition campaign consisting of three acquisitions for each damage scenario at the seven excitation levels has been performed. The resulting FRFs have been plotted as in Fig. 1, obtaining three images per scenario. The resulting images have been augmented according to the technique proposed in Sect. 4. In this way, $3^7 = 2187$ testing images were obtained per each scenario, for a total of 6561 images available for the test set. Therefore, we have two sets: set 0, the one used for training, and set 1, used for testing.

To include experimental data variability, tests have been performed with the same modalities but on different days. Such an additional response variation was crucial to preliminary assess the robustness of the IFDS. Indeed, due to the combined effects of friction and play within the pinned joints, the acquisition sets estimated on different days, after restarting the equipment, brought out a cluster effect. As an example, in Fig. 6, we plot the confidence band at 95% ($\pm 2\sigma$) of the FRF estimated ($Q_0 = 1$ N) in the scenario of loss of member connectivity along, set 0 and set 1, acquired on different days. Especially in the low-frequency region, it is clear how the variability induced by resetting the experiment is higher than the variance along consecutive measurements.

The cluster effect in Fig. 6 is also confirmed by quantitative evaluations based on a p-value test. In particular, two metrics were considered as the statistical test: z that is related to the difference between the average FRF: H_0 for set 0 and H_1 for set 1, and $z^{'}$ that is related to the difference between the average FRF slopes $H_0^{'}$ and $H_1^{'}$.

Given the confidence level α, the true hypothesis holds when:

$$\begin{aligned} z &= \frac{|H_1 - H_0|}{\sqrt{2\,\sigma_0^2}} \leq \tau_{1-\alpha/2} \\ z^{'} &= \frac{|H_1^{'} - H_0^{'}|}{\sqrt{2\,\sigma_0^{'2}}} \leq \tau_{1-\alpha/2} \end{aligned} \tag{3}$$

where: σ_0 and $\sigma_0^{'}$ stand for the standard deviation of H_0 and its slope $H_0^{'}$, respectively. In Eq. 3, $\tau_{1-\alpha/2}$ represents the threshold corresponding to the α confidence level.

If the hypothesis test does not hold, then there is statistical evidence that the two data sets are different. At this point, the scores p and $p^{'}$ can be computed as follows:

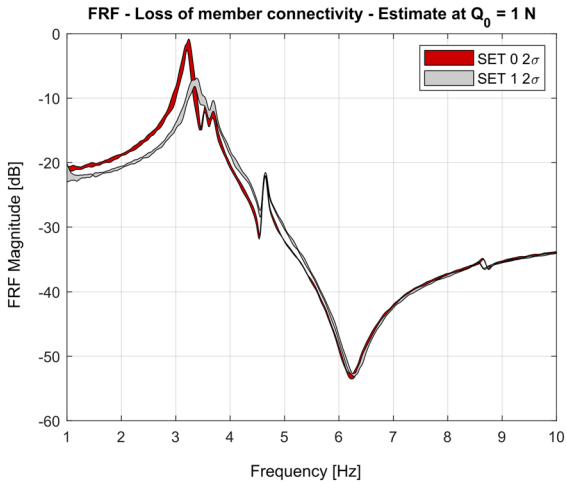

Fig. 6 The FRFs of two different acquisition sets of the loss of member connectivity scenario at $Q_0 = 1$ N. A clear cluster effect is shown due to changes in frictional conditions and joints play

Table 2 Average scores computed on the error on the FRF and FRF-derivative at 95% of confidence between set 0 and set 1, representing the difference between the testing set and the training set

Scenario	p	$p^{'}$
Undamaged	6.68	2.54
Loss of member connectivity	9.11	3.12
Reduction of artificial damping	7.36	4.33

$$p = \frac{\int \left(z - \tau_{1-\alpha/2}\right) df}{\Delta f}, \quad \text{for } z > \tau_{1-\alpha/2}$$
$$p^{'} = \frac{\int \left(z^{'} - \tau_{1-\alpha/2}\right) df}{\Delta f^{'}}, \quad \text{for } z^{'} > \tau_{1-\alpha/2} \tag{4}$$

In other words, such scores are the average computed over the frequency spectrum (0–10 Hz in this case) of the statistical test values that fall beyond the threshold $\tau_{1-\alpha/2}$. In Eq. 4, Δf and $\Delta f^{'}$ represent the amplitude of the frequency spectrum in which the statistical test z and $z^{'}$ exceed the threshold.

Such p-value tests were performed for each level of the excitation and each scenario (undamaged, loss of member connectivity, and reduction of artificial damping). Average results are listed in Table 2. According to the statistical band shown in Fig. 6, a confidence value of 95% was considered, i.e. $\tau_{1-\alpha/2} = 2$.

Results show that the two sets can be considered different based on both metrics. In particular, the null hypothesis for the z test was refuted for all scenarios over all the excitation levels. Instead, for the undamaged and loss of member connectivity scenarios, three levels of the excitation showed similarity between the data sets. Lastly, for the reduction of damping data, the null hypothesis on z' was rejected for all the excitation levels.

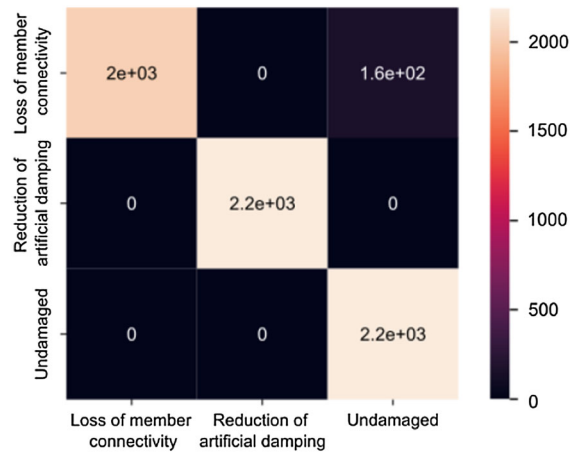

Fig. 7 Confusion matrix of the designed IFDS computed on the test set

5.4.3 Testing results

The resulting images were fed to the IFDS, obtaining a test accuracy of 97.6%. Figure 7, shows the corresponding confusion matrix. As can be seen, the IFDS struggles in correctly classifying some bolt damages that are actually classified as undamaged. Nevertheless, the designed IFDS has been able to overcome the cluster effect shown in Fig. 6, providing empirical support for the real-world application of the proposed method.

6 Ablation studies

To investigate the role of the key parameters of the proposed method, we propose the following ablation studies.

6.1 Excluding main faults features

To investigate the role of the main faults features in the design of the IFDS, we developed another IFDS,

Table 3 Test-accuracy of the IFDS trained using one excitation level and tested on the others

Test	1 N	3 N	5 N	7 N	9 N	11 N	13 N
Train							
1 N	66.6	11.1	22.2	11.1	22.2	33.3	33.3
3 N	44.4	88.8	77.8	44.4	44.4	22.2	11.1
5 N	66.6	66.6	55.6	55.6	66.6	33.3	55.6
7 N	33.3	33.3	33.3	55.6	55.6	44.4	44.4
9 N	22.2	66.6	44.4	88.8	66.6	55.6	66.6
11 N	55.6	33.3	33.3	44.4	55.6	55.6	77.8
13 N	33.3	22.2	11.1	55.6	66.6	66.6	44.4

The excitation level used for training is indicated on the rows of the table, while the excitation level used for testing is shown on the columns of the table

using the same architecture proposed in 5.4, but training it without using the frequency region containing main faults features. In this regard, we reduced the FRF data to a frequency interval located above 5 Hz. Such a choice is first motivated by the results of the theoretical modal analysis presented in Sec, 5.2. Indeed, the simulated damage scenarios are expected to modify the modal parameters of the undamaged structure only below 5 Hz, i.e. where the response is governed by the global mode shapes. Conversely, in the interval of 5–10 Hz, the effect of damages on the FRF is less evident, because the response is dominated by a structural mode at 8.7 Hz which is not altered by the simulated faults.

Such considerations are also reflected by the experimental estimates of the FRFs in Fig. 5, showing that the most significant damage signatures are located below 5 Hz. What is more, according to the p-value methodology discussed in Sect. 5.4, no significant difference emerged between the faults-datasets and the undamaged scenario above 7 Hz. Accordingly, the IFDS was executed on FRF-data limited to the interval 7–10 Hz. The outcome is that the accuracy of the IFDS drops to 34.5%, meaning that in this limited portion of the spectrum poor performance can be guaranteed in damage detection, compared when taking the entire frequency interval. The latter result confirms the importance of the damage signatures evidence in the design of the IFDS.

6.2 Removing data augmentation

To investigate the role of the data augmentation technique proposed in the design of the IFDS, we developed another IFDS, using the same architecture proposed in 5.4, but training it without augmenting the collected data in the first campaign, i.e. using the 9 images obtained, 3 per scenario. As done before, the final classifier fed with the features extracted by MobileNetV2 [33] and pre-trained on ImageNet [32] is trained for 20 epochs using Adam [17] as optimizer with a learning rate of 10^{-2} and then, the whole network is fine-tuned for 10 epochs with a learning rate of 10^{-5}.

The so-obtained IFDS scores 44.4% test accuracy, on the 9 images obtained during the second data collection campaign, the one done for testing purposes. For comparison, we report the test score obtained by the IFDS proposed in Sect. 5.4 on the same 9 images, which is 100%.

The conducted ablation study shows the importance of the proposed data augmentation technique in developing the IFDS: without its usage, the data available is not enough to provide the generalization capability needed by the IFDS to properly work in the real-world.

6.3 Using a single excitation level

To investigate the role of using multiple excitation levels in the technique proposed, we designed another IFDS, using the same architecture proposed in 5.4, but training without using both the visualization and augmentation technique proposed, i.e. using just the data collected at one excitation level, and testing on the other levels. As in the previous cases, training data belongs to the first data collection campaign (set 0), while testing data to the second (set 1).

Table 3 shows the test accuracies obtained by training the IFDS on the data collected at the excitation level indicated on the rows of the table and testing on the data collected at the excitation level listed on the columns of the table. The highest test accuracies appear on the diagonal of the table or in the immediately nearby. Such a phenomenon can be justified by the adjacency of the excitation levels used for training and testing. In general, the average accuracy obtained is significantly lower if compared to the one obtained by the proposed technique, thus, confirming the key role of nonlinearity in the proposed method, which overcomes the scarcity of data.

7 Conclusions

This document proposed a novel approach to tackle the problem of data scarcity often met during the design of IFDS. A multi-excitation level procedure leveraging intrinsic non-linearities of real-world systems is used to acquire and augment the available data, producing images that can be conveniently analysed by pre-trained Convolutional Neural Networks (CNNs) to diagnose faults. The proposed approach has been applied to designing an IFDS for the structural health monitoring of a real-scale railway pantograph. Three scenarios were studied: undamaged structure, a faulty bolted connection, and a faulty damper.

The designed IFDS was able to correctly classify 97.6% of the testing conditions, looking at the FRFs obtained at different excitation levels, showing a slight trend in misclassifying bolt damages as undamage condition. Nevertheless, the designed IFDS has been able to overcome the cluster effect shown by the pantograph's data acquired at different times, providing empirical support for the real-world application of the proposed method.

Acknowledgements The Authors would like to thank Trenitalia SpA for the support given during the development of the research activities.

Author contributions G.S. and A.M.G. equally contributed to the conceptualization of the method, the writing of the manuscript, and the editing of the figures. In particular, G.S. focused on the validation experiments while A.M.G. developed the software routine. M.S. and A.F. supervised the research activity.

Funding Open access funding provided by Scuola Superiore Sant'Anna within the CRUI-CARE Agreement. The Authors declare that no funds, grants, or other support were received during the preparation of this manuscript.

Data availibility The datasets generated and analysed during the current study are available from the corresponding Author on reasonable request.

Declarations

Conflict of interest The Authors declare that they have no Conflict of interest.

References

1. Ali, J.B., Fnaiech, N., Saidi, L., Chebel-Morello, B., Fnaiech, F.: Application of empirical mode decomposition and artificial neural network for automatic bearing fault diagnosis based on vibration signals. Appl. Acoust. **89**, 16–27 (2015)
2. An, F., Wang, J.: Rolling bearing fault diagnosis algorithm using overlapping group sparse-deep complex convolutional neural network. Nonlinear Dyn. **108**(3), 2353–2368 (2022)
3. Avci, O., Abdeljaber, O., Kiranyaz, S., Hussein, M., Gabbouj, M., Inman, D.J.: A review of vibration-based damage detection in civil structures: from traditional methods to machine learning and deep learning applications. Mech. Syst. Signal Process. **147**, 107077 (2021)
4. Biswas, M., Pandey, A.K., Bluni, S.A., Samman, M.M.: Modified chain-code computer vision techniques for interrogation of vibration signatures for structural fault detection. J. Sound Vib. **175**(1), 89–104 (1994)
5. CENELEC. Railway applications-current collection systems-requirements for and validation of measurements of the dynamic interaction between pantograph and overhead contact line, (2012)
6. CENELEC. Railway applications-current collection systems-validation of simulation of the dynamic interaction between pantograph and overhead contact line. (2018)
7. Chen, S., Ong, Z.C.: Waveform chain code: a more sensitive feature selection in unsupervised structural damage detection. In: 2019 1st International Conference on Artifi-

cial Intelligence and Data Sciences (AiDAS), pp. 116–119. IEEE (2019)
8. Chen, S., Ong, Z.C., Lam, W.H., Lim, K.-S., Lai, K.W.: Unsupervised damage identification scheme using PCA-reduced frequency response function and waveform chain code analysis. Int. J. Struct. Stab. Dyn. **20**(08), 2050091 (2020)
9. Chen, X., Li, X., Shupeng, Yu., Lei, Y., Li, N., Yang, B.: Dynamic vision enabled contactless cross-domain machine fault diagnosis with neuromorphic computing. IEEE/CAA J. Autom. Sinica **11**(3), 788–790 (2024)
10. Ewins, D.J.: Modal Testing: Theory Practice and Application. Wiley, London (2009)
11. Fang, Q., Dinghui, W.: Ans-net: anti-noise *siamese* network for bearing fault diagnosis with a few data. Nonlinear Dyn. **104**(3), 2497–2514 (2021)
12. Gao, D., Zhu, Y., Wang, X., Yan, K., Hong, J.: A fault diagnosis method of rolling bearing based on complex morlet cwt and cnn. In 2018 Prognostics and System Health Management Conference (PHM-Chongqing), pp. 1101–1105. IEEE, (2018)
13. Guo, S., Yang, T., Gao, W., Zhang, C.: A novel fault diagnosis method for rotating machinery based on a convolutional neural network. Sensors **18**(5), 1429 (2018)
14. He, F., Ye, Q.: A bearing fault diagnosis method based on wavelet packet transform and convolutional neural network optimized by simulated annealing algorithm. Sensors **22**(4), 1410 (2022)
15. Hou, R., Xia, Y.: Review on the new development of vibration-based damage identification for civil engineering structures: 2010–2019. J. Sound Vib. **491**, 115741 (2021)
16. MM Manjurul Islam and Jong-Myon Kim: Automated bearing fault diagnosis scheme using 2D representation of wavelet packet transform and deep convolutional neural network. Comput. Ind. **106**, 142–153 (2019)
17. Kingma, D. P., Ba, J.: Adam: A method for stochastic optimization. arXiv preprint arXiv:1412.6980, (2014)
18. Kopsaftopoulos, F.P., Fassois, S.D.: Vibration based health monitoring for a lightweight truss structure: experimental assessment of several statistical time series methods. Mech. Syst. Signal Process. **24**(7), 1977–1997 (2010)
19. Landauskas, M., Cao, M., Ragulskis, M.: Permutation entropy-based 2D feature extraction for bearing fault diagnosis. Nonlinear Dyn. **102**, 1717–1731 (2020)
20. Lee, D., Ahn, T.-S., Kim, H.-S.: A metric on the similarity between two frequency response functions. J. Sound Vib. **436**, 32–45 (2018)
21. Li, W., Huang, R., Li, J., Liao, Y., Chen, Z., He, G., Yan, R., Gryllias, K.: A perspective survey on deep transfer learning for fault diagnosis in industrial scenarios: theories, applications and challenges. Mech. Syst. Signal Process. **167**, 108487 (2022)
22. Li, X., Yu, S., Lei, Y., Li, N., Yang, B.: Intelligent machinery fault diagnosis with event-based camera. IEEE Transactions on Industrial Informatics (2023)
23. Li, X., Zhang, W., Xu L., Hao, H.: Partial domain adaptation in remaining useful life prediction with incomplete target data. IEEE/ASME Transactions on Mechatronics (2023)
24. Li, X., Li, J., Zhao, C., Yongzhi, Q., He, D.: Gear pitting fault diagnosis with mixed operating conditions based on adaptive 1D separable convolution with residual connection. Mech. Syst. Signal Process. **142**, 106740 (2020)
25. Li, Y., Minqiang, X., Wang, R., Huang, W.: A fault diagnosis scheme for rolling bearing based on local mean decomposition and improved multiscale fuzzy entropy. J. Sound Vib. **360**, 277–299 (2016)
26. Maria Pina Limongelli: The interpolation damage detection method for frames under seismic excitation. J. Sound Vib. **330**(22), 5474–5489 (2011)
27. Limongelli, M.P.: Frequency response function interpolation for damage detection under changing environment. Mech. Syst. Signal Process. **24**(8), 2898–2913 (2010)
28. Noël, J.-P., Kerschen, G.: Nonlinear system identification in structural dynamics: 10 more years of progress. Mech. Syst. Signal Process. **83**, 2–35 (2017)
29. Pandhare, V., Singh, J., Lee J.: Convolutional neural network based rolling-element bearing fault diagnosis for naturally occurring and progressing defects using time-frequency domain features. In: 2019 Prognostics and System Health Management Conference (PHM-Paris), pp. 320–326. IEEE, (2019)
30. Porcu, M.C., Patteri, D.M., Melis, S., Aymerich, F.: Effectiveness of the FRF curvature technique for structural health monitoring. Constr. Build. Mater. **226**, 173–187 (2019)
31. Prosvirin, A., Kim, J., Kim, J.: Bearing fault diagnosis based on convolutional neural networks with kurtogram representation of acoustic emission signals. In: Advances in Computer Science and Ubiquitous Computing: CSA-CUTE 17, pp. 21–26. Springer, (2018)
32. Russakovsky, O., Deng, J., Hao, S., Krause, J., Satheesh, S., Ma, S., Huang, Z., Karpathy, A., Khosla, A., Bernstein, M., et al.: Imagenet large scale visual recognition challenge. Int. J. Comput. Vision **115**, 211–252 (2015)
33. Sandler, M., Howard, A., Zhu, M., Zhmoginov, A., Chen, L-C.: Mobilenetv 2: inverted residuals and linear bottlenecks. In: Proceedings of the IEEE Conference on Computer Vision and Pattern Recognition, pp. 4510–4520 (2018)
34. Santamato, G., Chiaradia, D., Solazzi, M., Frisoli, A.: Detecting early damages in the railway pantograph mechanism: a multiple excitation approach for the frequency domain. Vehicle Syst. Dyn., pp. 1–22 (2023)
35. Santamato, G., Chiaradia, D., Solazzi, M., Frisoli, A.: A lightweight robotic device for the inspection of railway pantograph. In: 2019 IEEE International Symposium on Safety, Security, and Rescue Robotics (SSRR), pp. 284–289. IEEE, (2019)
36. Santamato, G., Chiaradia, D., Solazzi, M., Frisoli, A.: A lightweight robotic device based on a micro-macro actuation concept for the inspection of railway pantograph. J. Mech. Robot. **12**(6), 061002 (2020)
37. Santamato, G., Solazzi, M., Frisoli, A.: Investigating the effect of dry-friction on damage detection tests. J. Sound Vib. **568**, 117949 (2024)
38. Schoukens, J., Dobrowiecki, T., Pintelon, R.: Parametric and nonparametric identification of linear systems in the presence of nonlinear distortions—a frequency domain approach. IEEE Trans. Autom. Control **43**(2), 176–190 (1998)
39. Shao, H., Jiang, H., Lin, Y., Li, X.: A novel method for intelligent fault diagnosis of rolling bearings using ensemble

deep auto-encoders. Mech. Syst. Signal Process. **102**, 278–297 (2018)
40. Shao, H., Jiang, H., Zhang, H., Duan, W., Liang, T., Shuaipeng, W.: Rolling bearing fault feature learning using improved convolutional deep belief network with compressed sensing. Mech. Syst. Signal Process. **100**, 743–765 (2018)
41. Sun, Y., Li, S.: Bearing fault diagnosis based on optimal convolution neural network. Measurement **190**, 110702 (2022)
42. Sharif Uddin, M., Islam, S.A., Khan, J. K., Kim, J-M., Sohn, S-M., Choi, B-K., et al.: Distance and density similarity based enhanced-NN classifier for improving fault diagnosis performance of bearings. Shock Vib. 2016, (2016)
43. Verstraete, D., Ferrada, A., Droguett, E. L., Meruane, V., Modarres, M., et al.: Deep learning enabled fault diagnosis using time-frequency image analysis of rolling element bearings. Shock Vib. 2017, (2017)
44. Wang, C., Gan, M., Zhu, C.A.: A supervised sparsity-based wavelet feature for bearing fault diagnosis. J. Intell. Manuf. **30**, 229–239 (2019)
45. Wei, Yu., Yang, Y., Minqiang, X., Huang, W.: Intelligent fault diagnosis of planetary gearbox based on refined composite hierarchical fuzzy entropy and random forest. ISA Trans. **109**, 340–351 (2021)
46. Welch, P.: The use of fast Fourier transform for the estimation of power spectra: a method based on time averaging over short, modified periodograms. IEEE Trans. Audio Electroacoust. **15**(2), 70–73 (1967)
47. Wen, L., Gao, L., Li, X.: A new snapshot ensemble convolutional neural network for fault diagnosis. IEEE Access **7**, 32037–32047 (2019)
48. Worden, K., Tomlinson, G.R., Yagasaki, K.: Nonlinearity in structural dynamics: detection, identification and modeling. Appl. Mech. Rev. **55**(2), B26–B27 (2002)
49. Xia, M., Li, T., Lin, X., Liu, L., De Silva, C.W.: Fault diagnosis for rotating machinery using multiple sensors and convolutional neural networks. IEEE/ASME Trans. Mechatron. **23**(1), 101–110 (2017)
50. Xin, T., Roberts, C., Weston, P., Stewart, E.: Condition monitoring of railway pantographs to achieve fault detection and fault diagnosis. Proc. Inst. Mech. Eng. Part F J. Rail Rapid Transit **234**(3), 289–300 (2020)
51. Zhang, J., Sun Yi, G.U.O., Liang, G.A.O.H., Xin, H.O.N.G., Hongliang, S.O.N.G.: A new bearing fault diagnosis method based on modified convolutional neural networks. Chin. J. Aeronaut. **33**(2), 439–447 (2020)
52. Zhang, Q., Deng, L.: An intelligent fault diagnosis method of rolling bearings based on short-time fourier transform and convolutional neural network. J. Fail. Anal. Prev., pp. 1–17, (2023)
53. Zhang, W., Hao, H., Zhang, Y.: State of charge prediction of lithium-ion batteries for electric aircraft with swin transformer. IEEE/CAA J. Automat. Sinica, (2024)
54. Zhang, Y., Zhou, T., Huang, X., Cao, L., Zhou, Q.: Fault diagnosis of rotating machinery based on recurrent neural networks. Measurement **171**, 108774 (2021)
55. Zhao, Z., Qiao, B., Wang, S., Shen, Z., Chen, X.: A weighted multi-scale dictionary learning model and its applications on bearing fault diagnosis. J. Sound Vib. **446**, 429–452 (2019)
56. Zheng, J., Chen, Y., Pan, H., Tong, J.: Composite multiscale phase reverse permutation entropy and its application to fault diagnosis of rolling bearing. Nonlinear Dyn. **111**(1), 459–479 (2023)
57. Zhou, K., Diehl, E., Tang, J.: Deep convolutional generative adversarial network with semi-supervised learning enabled physics elucidation for extended gear fault diagnosis under data limitations. Mech. Syst. Signal Process. **185**, 109772 (2023)
58. Zuo, L., Fengjie, X., Zhang, C., Xiahou, T., Liu, Yu.: A multi-layer spiking neural network-based approach to bearing fault diagnosis. Reliab. Eng. Syst. Saf. **225**, 108561 (2022)